ARTICLE

Three-dimensional modeling of nanoconfined multiphase flow in clay nanopores using FIB-SEM images of shale

Xiangjie Qin, Han Wang, Yuxuan Xia, Wu He, Xuanzhe Xia, and Jianchao Cai*

*Correspondence: caijc@cup.edu.cn

Received: October 12, 2024; Accepted: November 7, 2024; Published Online: November 18, 2024; https://doi.org/10.59717/j.xinn-energy.2024.100050

GRAPHICAL ABSTRACT

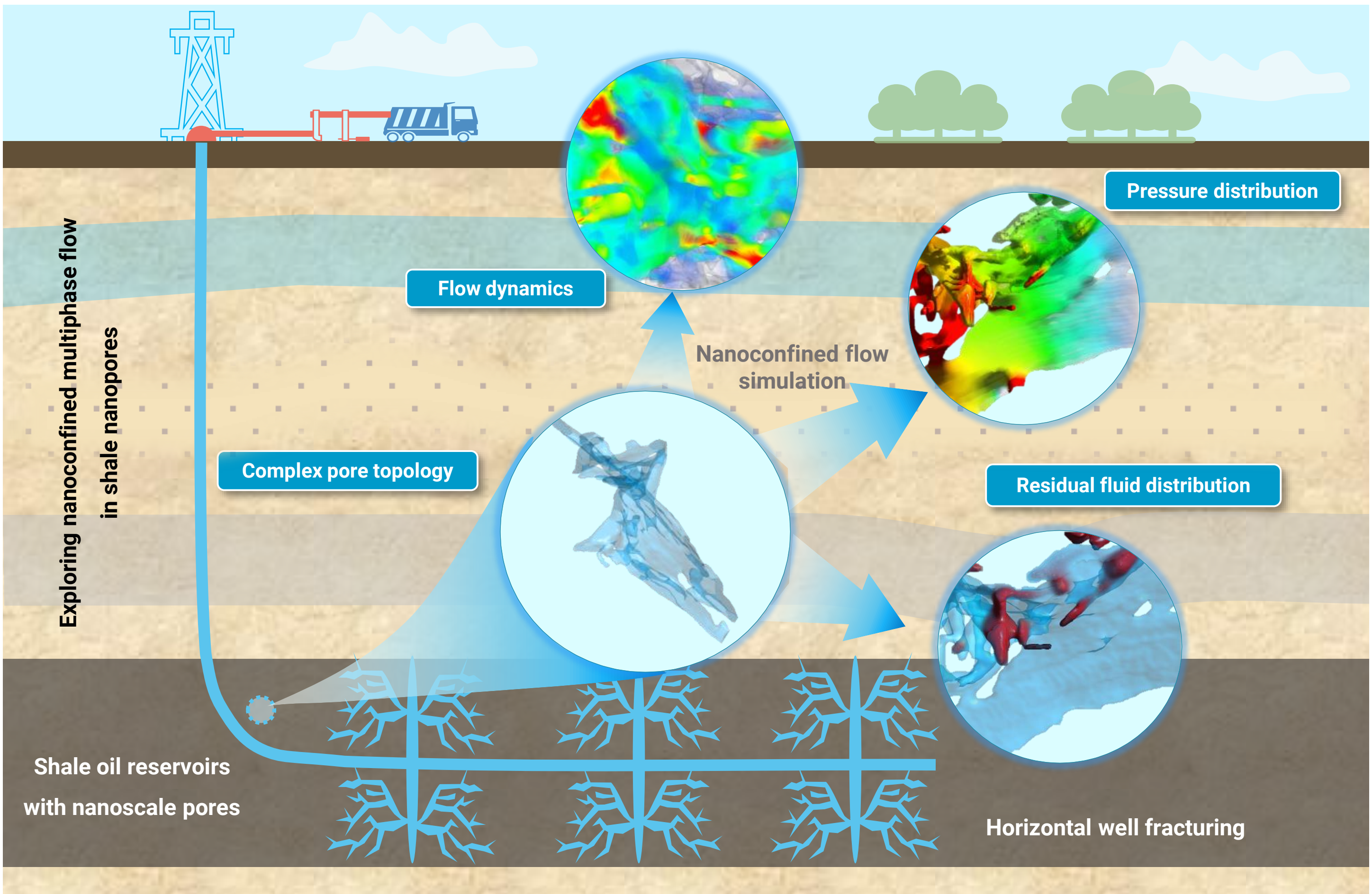

PUBLIC SUMMARY

- A pore-scale model is developed for slip flow in 3D shale nanopores.
- Imbibition rate increases and pressure decreases considering the nanoscale slip effect.
- Water flow is limited in clay nanopores and oil flow is enhanced.
- Capillary effect is enhanced in clay nanopores with low residual oil saturation.

ARTICLE

Three-dimensional modeling of nanoconfined multiphase flow in clay nanopores using FIB-SEM images of shale

Xiangjie Qin, Han Wang, Yuxuan Xia, Wu He, Xuanzhe Xia, and Jianchao Cai*

State Key Laboratory of Petroleum Resources and Engineering, China University of Petroleum, Beijing 102249, China

*Correspondence: caijc@cup.edu.cn

Received: October 12, 2024; Accepted: November 7, 2024; Published Online: November 18, 2024; https://doi.org/10.59717/j.xinn-energy.2024.100050

Citation: Qin X., Wang H., Xia Y., et al., (2024). Three-dimensional modeling of nanoconfined multiphase flow in clay nanopores using FIB-SEM images of shale. The Innovation Energy **1**(**4**): 100050.

Understanding the flow characteristics within shale nanopores is crucial for enhancing hydrocarbon recovery. However, the flow characteristics of wetting and non-wetting fluids on nanopore surfaces differ significantly, limiting the accurate prediction of hydrocarbon accumulation and migration. This work introduces the Euler-Euler volume of fluid method to establish a multiphase flow numerical model in shale nanopores, considering complex pore topology, slip flow, and capillary effects. Based on natural three-dimensional shale nanoporous systems constructed from FIB-SEM images, single-phase water/oil flow and water-oil forced imbibition simulations are carried out under the complete wetting condition. Results show that the displacement pressure is reduced and the imbibition rate is elevated considering nanoscale slip effects. As imbibition progresses, the pressure and imbibition rate gradually converge toward the values observed in conventional flows. In complete wetting nanoporous systems, water flow experiences high pressure and low velocity, whereas the pressure for oil flow is significantly reduced. Forced imbibition may undergo a transition from capillary force-dominated to viscous force-dominated, with a negative displacement pressure at the initial stage. Furthermore, the fluctuations in water-oil mass flow considering the slip effect are less pronounced than those observed in conventional flows, leading to reduced residual fluid saturation in blind-end pores and pore bodies caused by snap-off events. Pore systems with poor connectivity and narrow throat structures correspond to low displacement efficiency. The findings of this work explain the impact of nanoscale slip effects on flow characteristics in unconventional reservoirs, contributing to the reasonable assessment of fluid flow capacity and facilitating production planning.

INTRODUCTION

Shale oil and gas resources play a crucial role in energy exploration and development, particularly with the depletion of conventional hydrocarbon resources worldwide.[1,2] Shale contains a substantial number of microscale and nanoscale pores displayed in Figure 1, providing abundant space for fluid occurrence and migration.[3-5] Understanding the fluid flow process within confined nanoscale pores is challenging due to the complex pore topology,[6,7] microscopic force interactions, slip effect,[8,9] and wettability.[10,11] Especially in immiscible multiphase flow systems, each fluid exhibits distinct flow characteristics due to the differing interactions between wetting and non-wetting fluids with the pore surfaces. Therefore, the nanoscale flow differs from microscopic and Darcy scale flows, making conventional no-slip flows inapplicable.[12-14] However, these unique flow processes could be driven by different underlying pore-scale processes and mechanisms, which are yet to be explored and understood.

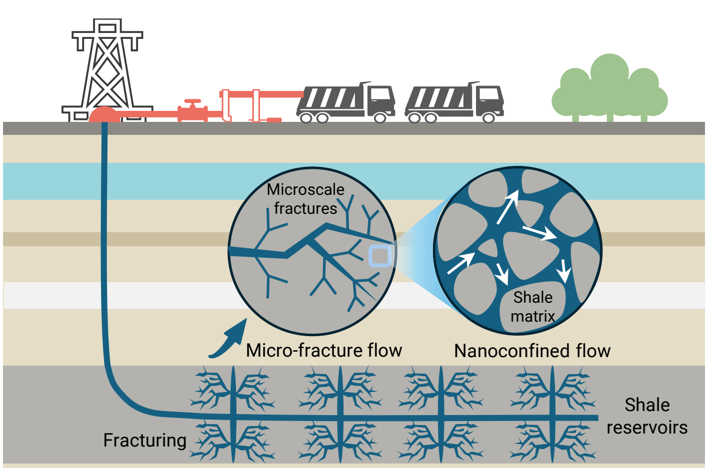

Figure 1. Nanoscale flow processes during shale oil development.

Adsorption and slip effects are critical mechanisms to consider in nanoconfined flow within shale reservoirs, with their impact diminishing as pore size increases.[15,16] For the adsorption effects, liquid molecules typically adhere to the surface of nanopores, resulting in a difference in viscosity between the adsorbed layer and the bulk region, thereby influencing the fluid flow within nanopores.[17,18] Slip means that liquid has a tangential velocity at pore surfaces which is determined by the strength of the fluid-solid interaction.[19] Wu et. al.,[20] obtained an exponential increase in enhancement factor with increasing contact angle in nanopores. Thus, fluid flow is typically enhanced when considering slip effects, whereas conventional simulations with no-slip conditions underestimate flow capacity,[21] particularly for the non-wetting fluid. Experimental methods obtain macroscopic flow properties and explore the fluid distribution by combining nuclear magnetic resonance equipment.[22,23] However, these methods are unable to quantify the micro- and nanoscale effects during the flow process. Nanofluidic chips provide the opportunity to experimentally investigate nanoscale flow behaviors and allow for the direct observation of complex flow phenomena under a microscope.[24] Zhang et. al.,[25] observed that the mass flow obtained from microchannel experiments exceeds the predictions of the no-slip theory, aligning with the results of the Maxwellian slip theory. Nanofluidic chips, which represent the complex pore topology of shale, are expensive to produce, and experimental conditions such as wettability and fluid properties are difficult to control. Molecular dynamics (MD) simulations are widely applied in slip flow within single nanopores.[26,27] However, it cannot capture flow characteristics within complex pore networks due to the large computation. In recent years, pore-scale simulations considering nanoscale effects have enabled the accurate prediction of complex flow behaviors in nanoporous media.[15,28] Direct numerical simulation (DNS) methods considering real pore topology and simplified equivalent pore network models (PNM) are two approaches for pore-scale modeling.[29-31] Yang et. al.,[32] developed an equivalent PNM for nanoconfined oil flow in shale considering the slip and adsorption effect. It was found that the apparent permeability is related to the slip distance, and the viscosity of the adsorbed layer has a negligible effect on shale oil flow. In comparison, DNS methods can capture the flow characteristics within real pore structures constructed based on high-resolution images, thereby restoring complex flow processes. Wang et. al.,[33] simulated nanoconfined water/oil flow in organic and inorganic nanopores based on lattice Boltzmann method (LBM) modified by MD simulation results. In addition, Qin et. al.,[34] constructed a heterogeneous wetting nanoporous medium containing clay, organic, and inorganic matter to investigate the water flow characteristics on different mineral surfaces. Consequently, DNS methods offer the possibility for describing complex flow behaviors in nanoporous media.

For immiscible two-phase flow, wetting and non-wetting fluids exhibit distinct fluid-solid interactions with shale nanopore surfaces.[35] The slip distance of wetting fluids is smaller due to strong fluid-solid interactions, whereas for non-wetting fluids, the slip distance is significant.[36] This leads to unique displacement patterns, interface dynamics, and residual fluid distribution.[37] However, conventional pore-scale simulation methods neglect the slip

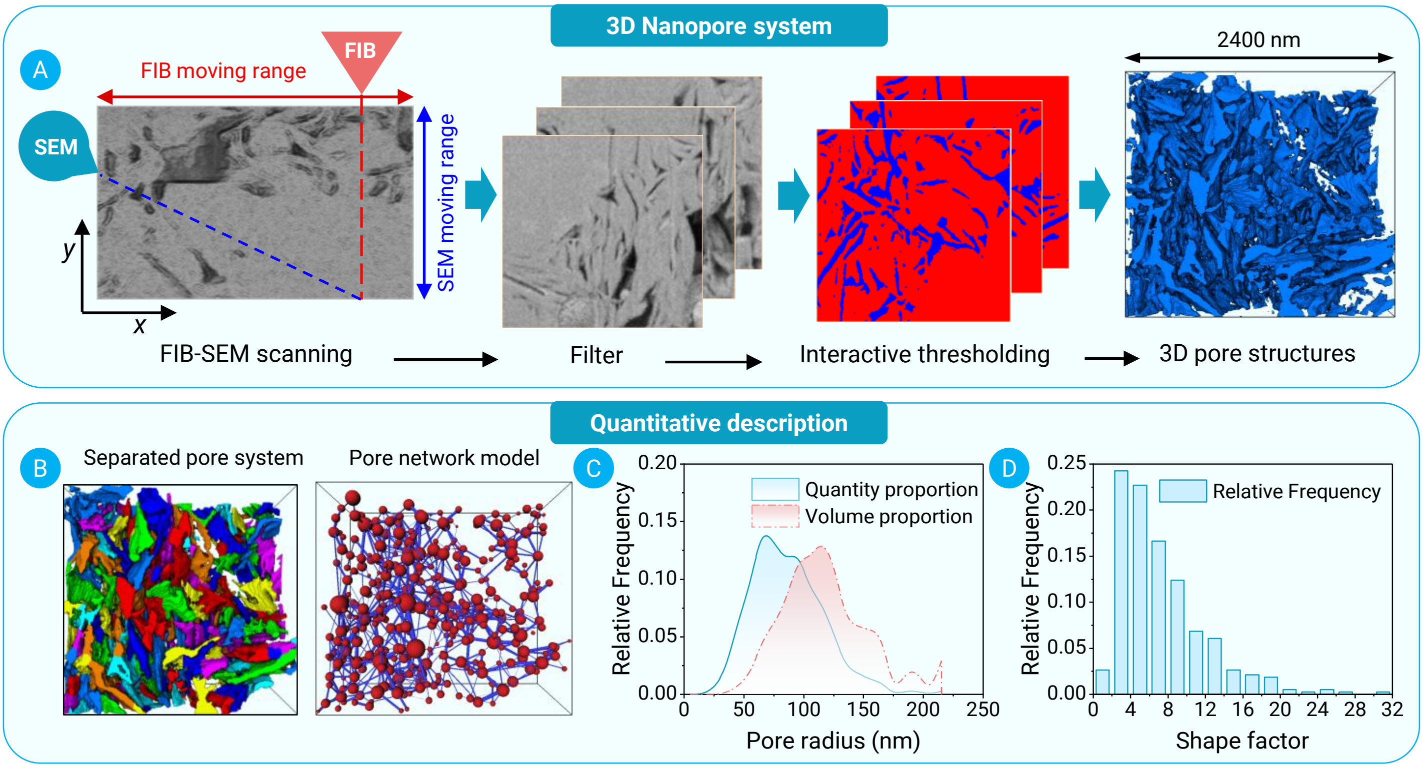

Figure 2. Establishing the 3D nanopore structures of shale (A) Image processing and reconstruction processes based on FIB-SEM images. (B) Generated PNM. (C) Nanopore size distribution. (D) Pore shape distribution.

effect of wetting and non-wetting fluids with pore surfaces,[38,39] which deviates from reality. Only a few studies have explored water-oil and gas-water slip flow within shale nanopores through pore-scale simulations. Zhang et. al.,[40] conducted water-oil flow simulations considering slip effects and effective viscosity based on the PNM of shale nanoporous system. The relative permeability of oil increases under slip conditions, but displacement efficiency decreases with increasing organic content. PNM can satisfactorily characterize macroscopic flow parameters such as relative permeability and capillary pressure curves. However, it fails to directly represent the two-phase interfaces and fluid distribution characteristics, which can be obtained from DNS methods. Zhang et. al.,[41] developed the pseudopotential-based LBM to simulate water-gas flow within shale nanopores considering fluid-fluid and fluid-solid interactions. For the water-oil flow behaviors, Wang et. al.,[42] improved the Multiple-Relaxation-Time LBM considering the liquid-liquid slip and liquid-solid slip effects. The velocity is enhanced significantly when considering the liquid-solid effect, while the influence of liquid-liquid slip on water-oil flow is minimal. Therefore, the influence of liquid-solid slip on immiscible two-phase flows is not disregarded in nanoporous media.

Existing DNS methods for solving nanoconfined multiphase flow primarily focus on two-dimensional (2D) porous media, which fail to capture the heterogeneous pore structures of shale due to the complex mineral composition. Three-dimensional (3D) pore filling mechanisms, two-phase interfaces, and residual fluid distribution are different from 2D perspectives, especially for imbibition processes under the complete wetting condition. Furthermore, the interactions of capillary and viscous forces in nanoconfined pore spaces are complex due to the slip effect, and the underlying mechanisms remain poorly understood.

In this context, this work introduces the Euler-Euler volume of fraction (EE-VOF) method with a fluid-dependent boundary to consider the slip effects of wetting and non-wetting fluids, enabling direct simulations of multiphase flow in complex 3D shale nanopores. Firstly, the spontaneous imbibition processes are compared under slip and no-slip conditions in different capillaries to verify the reliability of the method. Then, 3D shale nanoporous systems are reconstructed based on focused ion beam-scanning electron microscope (FIB-SEM) images, and simulations of single-phase water/oil flow, as well as water-oil two-phase flow, are conducted within complete wetting nanoporous systems. Finally, the microscopic force interactions and pore filling mechanisms are analyzed through the variation of injection pressure and water-oil flow rates during forced imbibition, and the influence of complex pore topology on residual oil distribution and interface curvature is clarified.

MATERIALS

Shale sample

The shale sample from Niuzhuang Well with a burial depth of 3574 m in Jiyang Depression is selected as the benchmark. The permeability obtained through the pulse attenuation method is 0.00018 mD, indicating that the rock possesses an ultra-low permeability. The mineral composition is determined using X-ray diffraction, revealing that the clay mineral, abundant in nanoscale pores, is predominant at 47.9%, followed by quartz and calcite at 24.0% and 20.1% respectively. Additionally, the total organic carbon content is 3%. For the pore structure properties, the porosity obtained through high-pressure mercury intrusion is 7.4%, with the advancing and retreating mercury curves indicating poor connectivity. The high-pressure mercury intrusion results reveal that the volume percentage of micropores (<2 nm) and mesopores (2-50 nm) is 21.44%. Therefore, boundary slip significantly affects fluid flow within the shale reservoirs. It is necessary to clarify the nanopore structures of shale and investigate the single-phase and two-phase flow behaviors in nanopores.

3D reconstruction of shale nanoporous structures

To obtain the 3D nanopore structures of shale, the FIB-SEM scanning experiment is conducted using the Helios NanoLab 660 manufactured by FEI Corporation. The extraction of shale nanopores is accomplished following the process depicted in Figure 2A. The FIB system generates ion beams for sample cutting, while the SEM system is used for real-time imaging. During scanning, select the areas with developed nanoscale pores for 3D imaging. The imaging area features a widespread distribution of clay mineral pores with effective connectivity. The scanning resolution and the sample cutting interval are both set at 10 nm. After the scanning is completed, a series of pre-processing steps are applied to the images to enhance quality. Specifically,

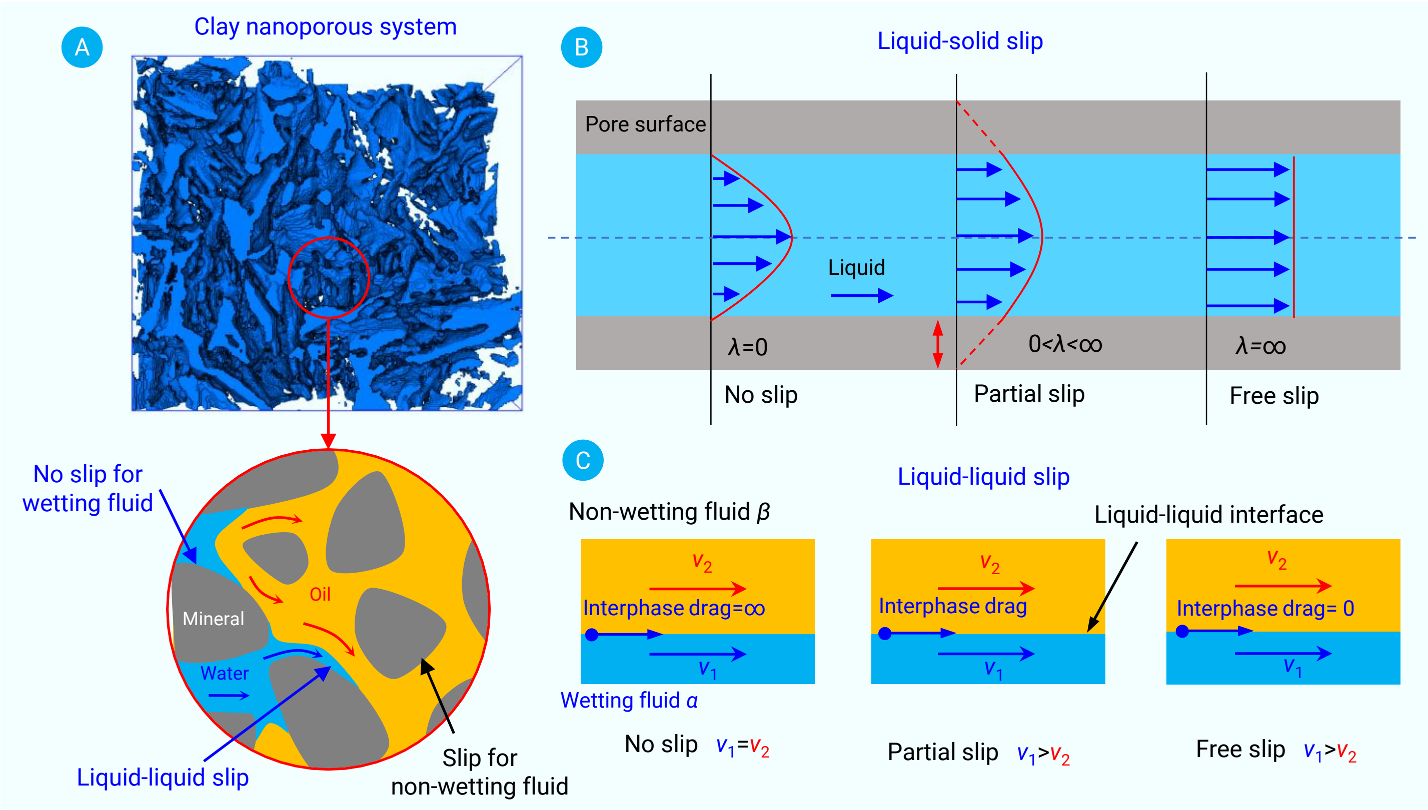

Figure 3. Water-oil flow mechanisms in shale nanopores (A) Two-phase flow in shale nanoporous system; (B) Liquid-solid slip and (C) liquid-liquid slip mechanisms in nanopores.

background correction is performed on the aligned grayscale images to eliminate shadows. The Fast Fourier Transform (FFT) algorithm is used to remove stripe noise caused by periodic distributions in the images. Additionally, a method that combines grayscale value-based interactive threshold segmentation with top-hat segmentation based on image brightness is employed to extract pore structures. Subsequently, algebraic addition is applied to merge the segmentation results and obtain 3D shale pore structures.

3D imaging methods have unique advantages in quantitatively characterizing pore shape and topology. Distance transformation is applied to the segmented image to generate a distance map, and then the watershed algorithm is utilized to segment pore spaces as illustrated in Figure 2B, ultimately creating the pore network model. Figure 2C counts the pore number and volume distribution characteristics. The pore number exhibits a unimodal distribution, with pore radius concentrated in the range of 65-95 nm, accounting for 51.7% of the total. Pore volume shows a roughly bimodal distribution, with the volume proportion of pores in the radius range of 95-125 nm accounting for 48.47%. Figure 2D shows that the shape factor is concentrated in the range of 2-9, accounting for 75.99% of the total, with the majority of pores exhibiting a plate-like shape.

METHODS

The slip effect is significant for oil flow in shale nanopores, due to the strongly hydrophilic pore surfaces of clay minerals. The impact of heterogeneous viscosity caused by adsorption layers within the pore diameter range is negligible according to previous studies.[20,32,34] Therefore, the heterogeneous viscosity is not considered in simulations. The Navier-Stokes equation considering slip effect (i.e. Navier slip model) is the governing equation for single-phase flow. Additionally, the EE-VOF method is introduced for the simulation of immiscible two-phase flow in nanoporous systems.[43]

Immiscible multiphase transport in complex pore-throat systems

Considering the nanoscale slip effect, it is necessary to solve the velocity fields of wetting and non-wetting phases separately. Conventional VOF methods are unsuitable for nanoscale slip flows due to the shared velocity fields of the two-phase fluids. For inhomogeneous multiphase flows, the EE-VOF method solves the velocity fields of two-phase fluids separately in the momentum equation:

$$\frac{\partial(r_a\rho_a\vec{u}_a)}{\partial t}+\nabla\cdot(r_a\rho_a\vec{u}_a\vec{u}_a)=-r_a\nabla p+\nabla\cdot(r_a\mu_a(\nabla\vec{u}_a+\nabla\vec{u}_a^T))+\vec{F}_{si}+\vec{F}_{di} \quad (1)$$

where r_a, ρ_a, μ_a, and $\vec{u}_a$ are the volume fraction, density, viscosity, and velocity of phase a, t is the computation time, p is the pressure shared by all phases, $\vec{F}_{si}$ is the surface tension force, and $\vec{F}_{di}$ is the interfacial drag force.

The continuity equation follows:

$$\frac{\partial(r_a\rho_a)}{\partial t}+\nabla\cdot(r_a\rho_a\vec{U}_a)=0 \quad (2)$$

The sum of the volume fractions of all phases is 1. Dividing Equation (2) by the phase density and adding all phases yields the transported volume conservation equation:

$$\sum_a\frac{1}{\rho_a}\left(\frac{\partial(r_a\rho_a)}{\partial t}+\nabla\cdot(r_a\rho_a\vec{U}_a)\right)=0 \quad (3)$$

The interfacial drag force ($\vec{F}_{di}$), which describes the strength of liquid-liquid slip, is determined by the velocity difference of the two-phase fluids and the drag coefficient. The continuum surface force model is introduced to calculate surface tension force ($\vec{F}_{si}$), which makes surface tension force as a volume force concentrated at the interface.[44] Wall adhesion is considered by specifying the contact angle, without accounting for contact angle hysteresis. The calculations of interface curvature and the surface tension force must satisfy the contact angle. Consequently, according to the momentum and mass conservation equations, the velocity, volume fractions of two-phase fluids and shared pressure field can be obtained. In addition, the free surface model is introduced to resolve the interface between the fluids. To obtain a sharp interface, a compressive differencing scheme is adopted for the advection of volume fractions in the volume fraction equations, and the pressure gradient is processed to ensure that the flow is well maintained at the interface.

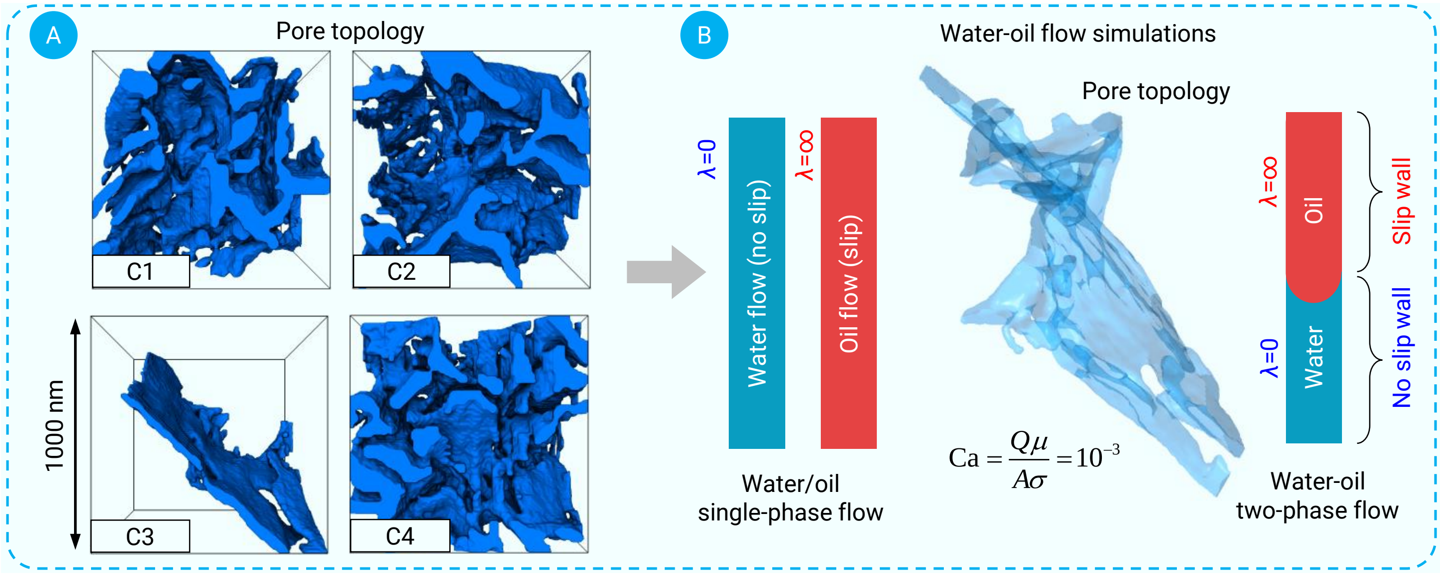

Figure 4. Simulation and analysis process (A) Subdomains with complex pore topology; (B) Slip conditions for single-phase and water-oil two-phase flow simulations.

Treatment of slip flows

Liquid-solid and liquid-liquid slip may occur in two-phase flow systems in the way demonstrated in Figure 3A. Liquid-solid slip refers to the tangential velocity of wetting and non-wetting fluids on pore surfaces due to wettability. Figure 3B illustrates the no-slip, partial slip, and free slip conditions for liquid-solid slip flows. The no-slip condition means that the tangential velocity of the fluid on pore surfaces is zero, which is the setting for conventional flows. Partial slip indicates the existence of tangential velocity at pore surfaces. However, free slip means that the fluid flow is not restricted by pore surfaces. The greater the contact angle, the more significant the slip effect is. The slip distance (λ) is a function of contact angle:[45]

$$\lambda = \frac{C}{(\cos\theta + 1)^2} \tag{4}$$

where θ is the contact angle, and C is a constant, determined to be 0.41 through MD simulation data.

The slip distance within nanoscale pores is close to or even much greater than the pore radius. It is necessary to consider fluid-solid slip in nanoscale multiphase flows. Fluid-dependent wall boundary condition is introduced for the slip flow, which allows setting up wall conditions for different fluids separately.

For two-phase stratified flows, liquid-liquid slip can be described through interphase drag force ($\vec{F}_{di}$), which is the total drag exerted by phase α on phase β per unit volume:

$$\vec{F}_{di} = C_{\alpha\beta}(\vec{u}_\alpha - \vec{u}_\beta) \tag{5}$$

where $C_{\alpha\beta}$ is a coefficient related to the dimensionless drag coefficient (C_D), which characterizes the degree of liquid-liquid slip:[46]

$$C_D = \frac{2D}{\rho_\alpha(\vec{u}_\alpha - \vec{u}_\beta)^2 A} \tag{6}$$

where D is the magnitude of the drag force, and A is the interface contact area.

Liquid-liquid slip is also divided into no-slip, partial slip, and free slip, as displayed in Figure 3C. The no-slip condition means that the interphase drag force between phases is infinite and the movement of the two phases is consistent. The partial slip condition indicates the relative motion of the two phases driven by the interphase drag force. Free slip condition means that there is no momentum transfer between the two phases, and the two-phase flows are independent. The degree of liquid-liquid slip is related to Reynolds number ($Re_{\alpha\beta}$), which physically represents the ratio of inertial force and viscous force:

$$Re_{\alpha\beta} = \frac{\rho_{\alpha\beta}\left|\vec{u}_\beta - \vec{u}_\alpha\right| d}{\mu_{\alpha\beta}} \tag{7}$$

where d is the characteristic length (i.e. capillary diameter), $\rho_{\alpha\beta}$ and $\mu_{\alpha\beta}$ are the mixture density and viscosity, which are obtained by weighted averaging, $\rho_{\alpha\beta} = r_\alpha\rho_\alpha + r_\beta\rho_\beta$, $\mu_{\alpha\beta} = r_\alpha\mu_\alpha + r_\beta\mu_\beta$.

The interphase drag coefficient is negatively correlated with Reynolds number. The inertial force affects fluid flow more strongly than the viscous force at high Reynolds numbers, resulting in a large interface momentum loss and significant liquid-liquid slip. However, microscale and nanoscale flows behaved as laminar flows are dominated by viscous forces at low Reynolds numbers, with significant interface momentum transfer. Therefore, liquid-liquid slip slightly affects multiphase flow at the nanoscale and is neglected in the simulations. In addition, the degree of liquid-liquid slip is controlled by multiple factors such as capillary diameter, droplet shape, and interface area, and the drag coefficient is difficult to estimate in complex pore structures.

Simulation schemes and processes

Due to the expensive computation of the original model, four cubic subdomains, with the pore topology displayed in Figure 4A, are extracted for simulations. Under the slip conditions, single-phase flow simulations for both water and oil, as well as water-oil two-phase flow simulations, are conducted separately, as shown in Figure 4B. Due to the strong hydrophilicity of clay minerals, simulations are conducted under the complete wetting condition to highlight the nanoscale slip effect. According to Equation (4), the slip distance of wetting fluid is defined as zero, indicating no-slip flow for water. In contrast, the slip distance for the oil phase is infinite, allowing free slip flow on pore surfaces. In addition, Zhao et. al.,[47] demonstrated that the slip effect is significant in microscale pores when the contact angle is 150°. Therefore, the slip effect in nano- and submicropores is non-negligible under the complete wetting condition. Fluid-dependent boundary conditions are introduced to define the slip flow of wetting and non-wetting fluids separately. In addition, flow characteristics as well as the residual fluid distribution are compared under different slip conditions, aiming to clarify the impact of complex pore topology on fluid flow and recovery efficiency.

To facilitate computation, the geometric model is meshed to discretize the computational domain. Tetrahedral grids are utilized to better accommodate complex pore topology. The number of grids is determined to be approximately 1,500,000 through mesh independence analysis, with a relative error of less than 5%. The calculation residual is set to 10^{-6}, and the computation stops when the convergence target is reached. Flow parameters are set based on the capillary number (Ca), which non-dimensionalizes the effects of viscosity and capillary forces:

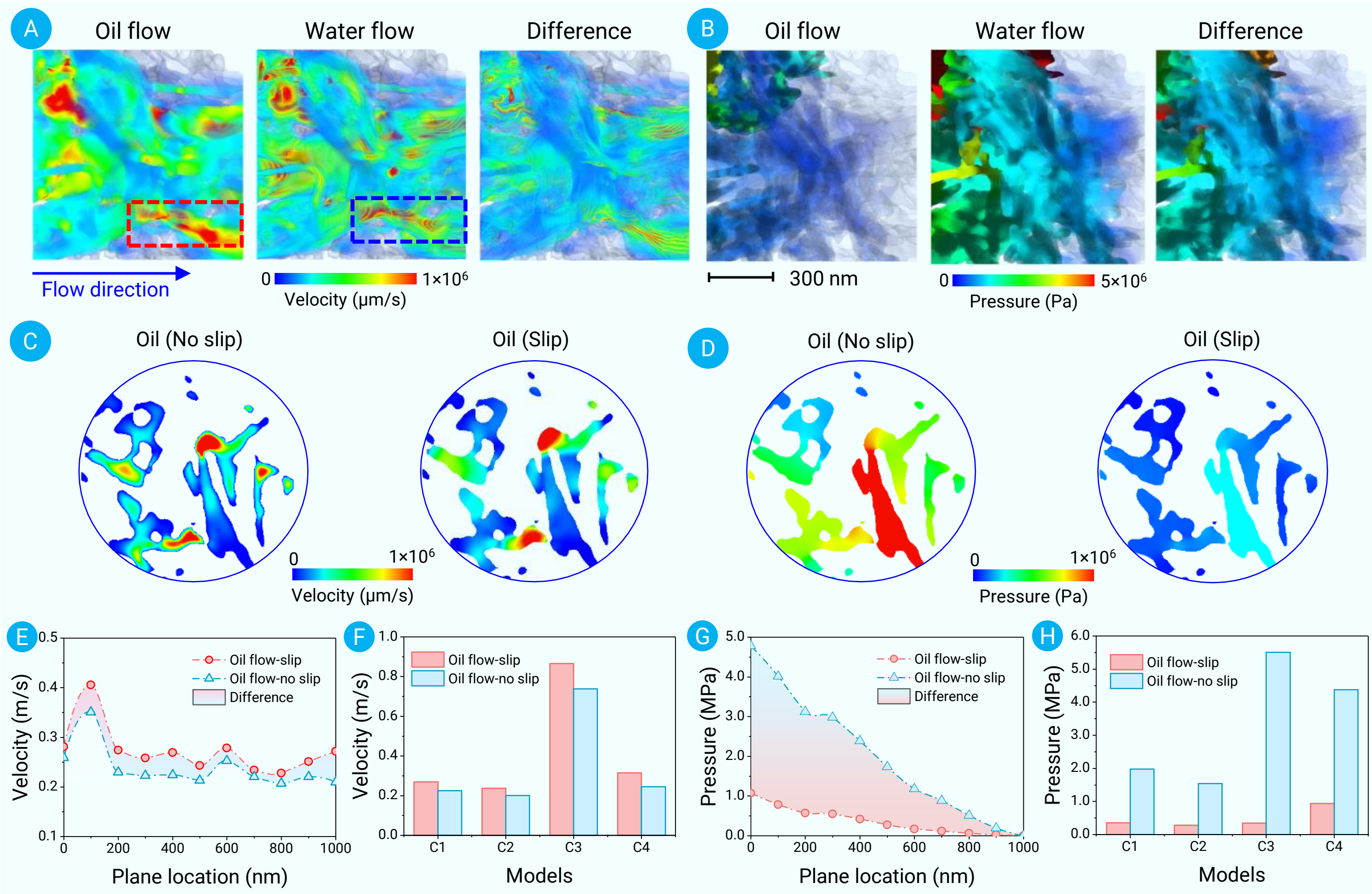

Figure 5. Velocity and pressure distribution characteristics for single-phase water and oil flow in nanoporous media Volume rendering of (A) velocity and (B) pressure distribution. (C) Velocity and (D) pressure distribution within the planes. (E) Variation of velocity along the flow direction. (F) Average velocity within different models. (G) Variation of pressure along the flow direction. (H) Average pressure within different models.

$$Ca = \frac{Q\mu}{A\sigma} \tag{8}$$

where Q is the volume flow rate, A is the cross-sectional area, μ is the viscosity of the invading fluid, and σ is the interfacial tension.

Simulations are conducted at a capillary number of 10^{-3}, corresponding to a volume flow rate of 4.8×10^{-14} m^3/s. To replicate water-oil flow processes under reservoir conditions, the viscosity of crude oil is tested under the reservoir temperature (130 ℃) for numerical simulations. The viscosities of water and oil are set at 0.001 and 0.0014 Pa·s respectively. The densities of water and oil are 1000 and 800 kg/m³ respectively. Water-oil interfacial tension coefficient is 0.048 N/m.

The transport equations are discretized using the second-order backward Euler method within the CFX solver manager, which offers high precision. Additionally, a pseudo-transient solution scheme with adaptive time steps is introduced to solve the complex flow behaviors in heterogeneous pore structures. Smaller time steps are used to ensure accuracy in unstable flows, whereas larger time steps are employed for stable flows to optimize computational efficiency.

RESULTS AND DISCUSSION

Water-oil slippage flow in capillaries

Simulations of spontaneous imbibition are performed in a circular capillary with a diameter of 1000 nm and a square capillary with a side length of 1000 nm in Figure S1A to validate the water-oil slip flow, where water and oil are assigned consistent viscosity and density values. The capillary has a length of 20000 nm, with one end connected to the wetting fluid and the other end connected to the non-wetting fluid. The initial liquid height of the wetting fluid is 1000 nm, and it spontaneously rises under the effect of capillary force. The Lucas-Washburn equation is introduced to validate the spontaneous imbibition process under the no-slip condition and to compare it with the simulation results under the slip condition. When gravity is neglected, the relationship between the imbibition height (l) of the wetting fluid inside a capillary and the time (t) is as follows:[48,49]

$$\frac{\mu_w - \mu_n}{2}(l^2 - l_0^2) + \mu_n L(l - l_0) = \frac{R\sigma\cos\theta}{6}t \tag{9}$$

where μ_w and μ_n represent the viscosity of the wetting and non-wetting fluids, L and R represent the length and radius of the capillary, and l_0 represents the initial liquid height of the wetting fluid.

It is known that the water saturation increases linearly with imbibition time under the no-slip condition. As displayed in Figure S1B & C, the numerical simulation results are consistent with the theoretical predictions (Equation (8)), indicating that the surface tension model for water-oil flow is reasonable. However, under slip conditions, the wall in contact with the oil phase is defined as a free slip boundary. Consequently, the mobility of oil is enhanced, resulting in an accelerated rise in water saturation. Especially in the initial imbibition stage, the contact area between the oil phase and pore surfaces is large, leading to a significant increase in the imbibition rate. As the imbibition progresses, oil is gradually displaced, and the imbibition rate decreases gradually.

The capillary forces of circular and square capillaries can be calculated as follows:[50]

$$P_c = \frac{2\sigma\cos\theta}{R} \tag{10}$$

$$P_s = 2\sigma\left(\frac{1}{h} + \frac{1}{w}\right)\cos\theta \tag{11}$$

Table 1. Absolute and apparent permeability of models.

Samples	Absolute permeability (mD)	Apparent oil permeability (mD)	Enhancement factor
C1	1.46E-2	6.48E-2	4.44
C2	1.81E-2	9.15E-2	5.06
C3	5.63E-3	5.09E-2	9.04
C4	4.44E-3	1.81E-2	4.08

where P_c and P_s respectively represent the capillary forces of circular and square capillaries, and h and w are the height and width of the rectangular cross-section, respectively.

Significantly, the imbibition rate in the square capillary is lower than that in the circular capillary (Figure S1C). This is because the capillary forces for circular and square capillaries are equal according to Equations (9) & (10). However, the square capillary has a larger pore volume, leading to a lower imbibition rate. Additionally, due to the larger capillary forces at the corners in rectangular capillaries, the wetting fluid displaces the non-wetting fluid in a corner flow manner. Figure S1D presents the variation in inlet pressure under slip and no-slip conditions. The inlet pressure for slip flows remains negative and the inlet pressure is relatively stable under the no-slip condition. As non-wetting fluid is gradually displaced, the inlet pressure tends to equalize under both slip and no-slip conditions.

Water/oil single-phase flow in the nanoporous system

Due to the fluid-solid interactions, fluid flow exhibits significant differences between wetting and non-wetting surfaces. Figures 5A & B compare the velocity and pressure distributions in single-phase water and oil flows. Under complete wetting conditions, the flow of oil, as a non-wetting fluid, is significantly enhanced; meanwhile, the flow of water is restricted due to the affinity of pore surfaces. Both water and oil exhibit higher flow velocities in narrow channels. Through comparison, the velocity field of oil is widely distributed, while the velocity of water is suppressed at pore surfaces due to the strong affinity. The pressure of water and oil gradually decreases along the flow direction, with relatively high pressure observed in blind-end pores. Besides, the pressure of non-wetting fluid is extremely low for enhanced fluidity.

The flow characteristics of oil under slip and no-slip conditions are compared. As displayed in Figure 5C, the velocity of oil constrained by pore surfaces is lower, while the velocity is higher in the center of the pore body under the no-slip condition. In contrast, oil is essentially free from the constraints of pore surfaces considering the slip effect, resulting in higher velocities at pore surfaces. Fluid pressure, as displayed in Figure 5D, drops significantly considering the slip effect because the oil is less constrained by the pore surfaces. Consequently, the oil velocity under the slip condition is higher within the internal planes as shown in Figure 5E. Due to the differences in pore structure properties, the velocity is higher than that under no-slip conditions to varying degrees in Figure 5F. Besides, the pressure decreases gradually along the flow direction. There is a notable contrast in oil pressure under slip and no-slip conditions in Figure 5G. The inlet pressure considering slip effects is reduced by 4.7 times compared to no-slip flows. Similarly, the fluid pressure corresponding to slip flow is lower than that of no-slip flow to varying degrees within the simulated models, as shown in Figure 5H. In addition, the absolute permeability and apparent oil permeability of the models are calculated (Table 1). Despite the strong connectivity of clay pores, the absolute permeability is extremely low due to their narrow pore throat sizes, ranging from 5.63E-3 mD to 1.81E-2 mD. The apparent oil permeability is significantly higher than the absolute permeability, with enhancement factors ranging from 4.08 to 9.04.

Forced imbibition in shale nanoporous system

Microscopic force interactions and pore-filling mechanisms. Based on the pseudo-transient solution scheme, the changes in inlet pressure and water-oil volume flow rate as time progresses have been recorded in Figure 6. The inlet pressure reflects internal flow characteristics; significant fluctuations represent complex interface dynamics. In nanoporous systems, the variation trend of inlet pressure displayed in Figure 6A roughly corresponds to that in capillaries under slip and no-slip conditions. The inlet pressure approaches stability under no-slip conditions; whereas the inlet pressure initially rises and then stabilizes under slip conditions. This means that the viscous force dominates the displacement process over the capillary force under the no-slip condition. Additionally, the inlet pressure may be negative under slip conditions during the initial stage of forced imbibition, indicating that capillary forces dominate the displacement process, while external forces act as the resistance to imbibition. However, influenced by the viscous force and complex pore topology, the inlet pressure gradually increases and exceeds zero during the imbibition process. This indicates that external force drives the forced imbibition, with displacement governed by both capillary

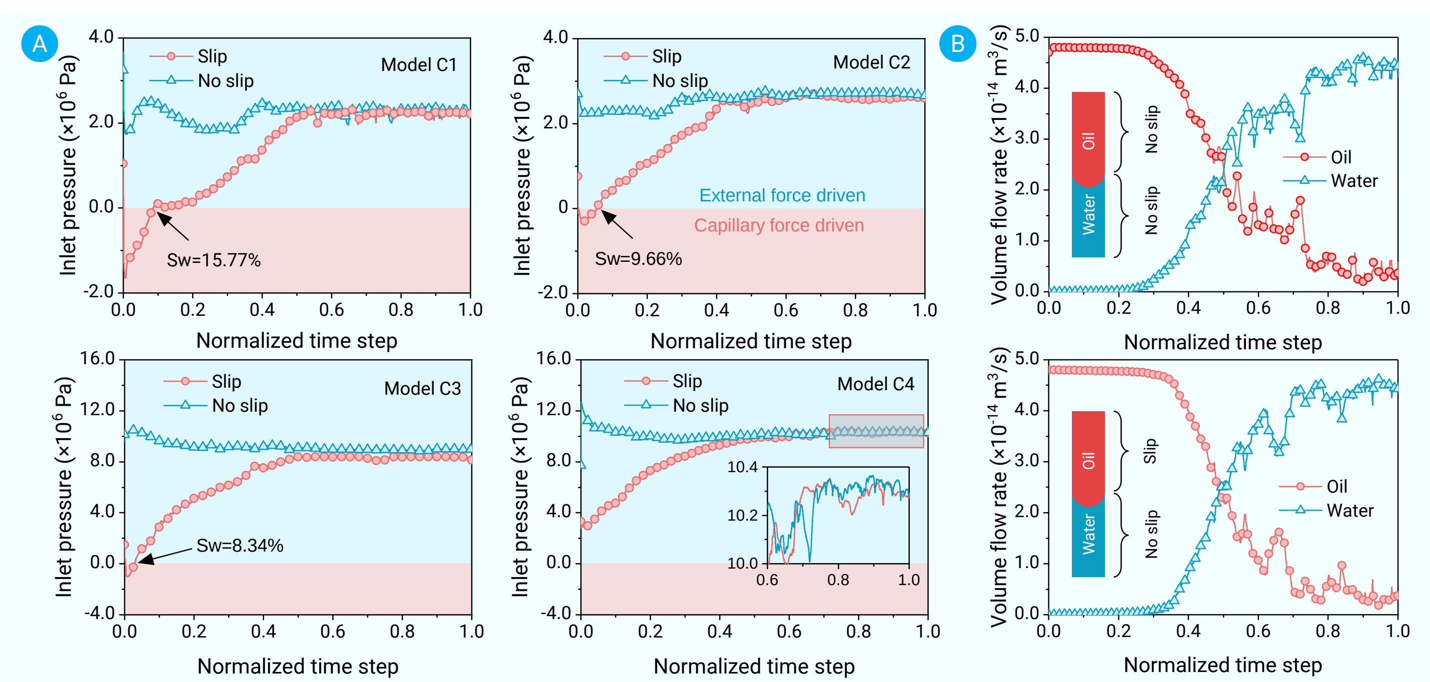

Figure 6. Variation of inlet pressure and water-oil volume flow rate under slip and no-slip conditions (A) Inlet pressure. (B) Water-oil volume flow rate.

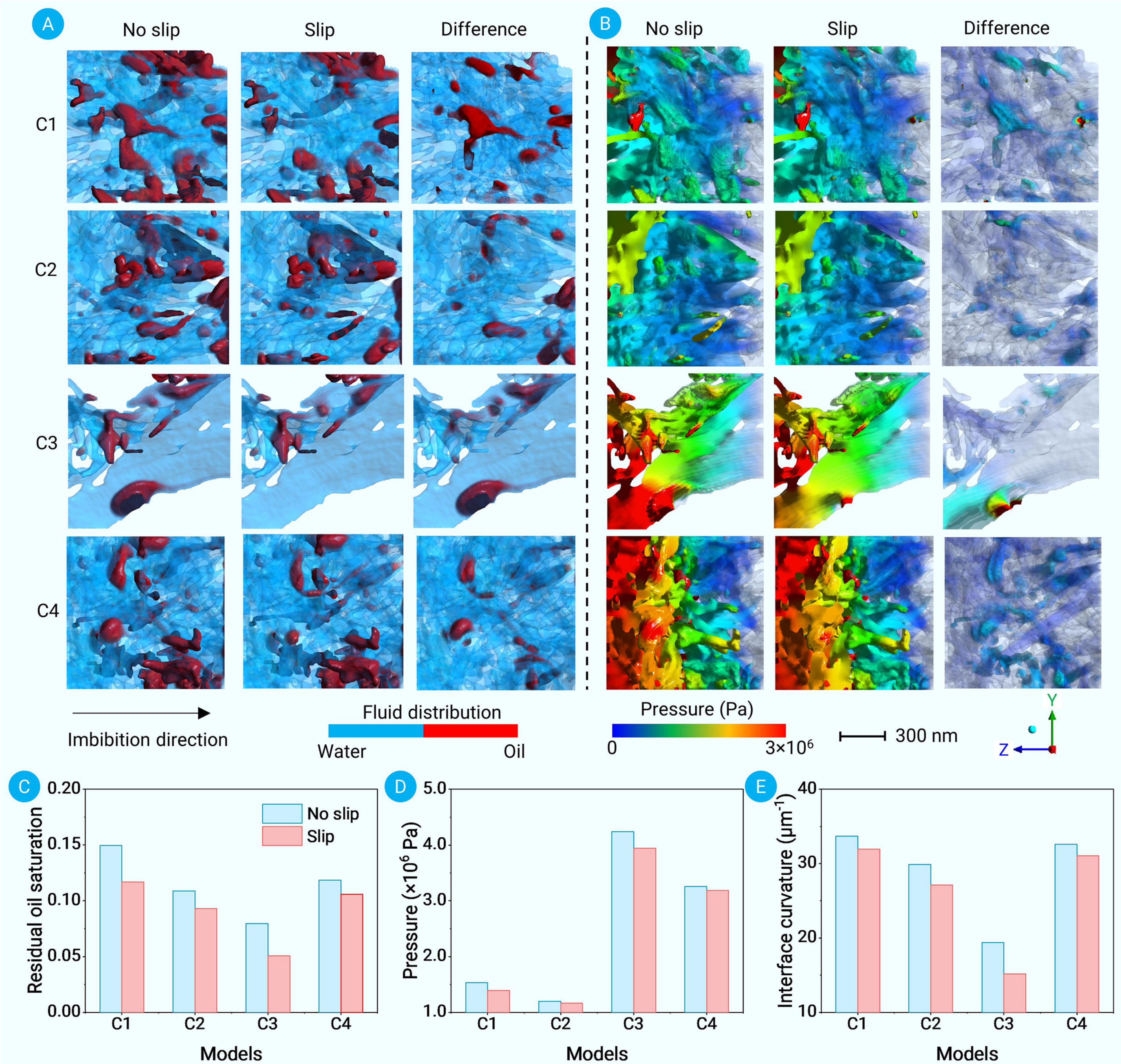

Figure 7. Residual fluid and pressure distribution characteristics in nanoporous systems Comparison of (A) residual fluid and (B) pressure distributions under slip and no-slip conditions. (C) Residual oil saturation, (D) fluid pressure, and (E) average interface curvature under slip and no-slip conditions.

and viscous forces. The inlet pressure of model C4 remains positive under the slip condition, possibly due to its complex pore structures. The entire displacement process is predominantly governed by viscous force. Combining the research of Liu et. al.,[51] it is found that the microscopic force interactions in nanoporous media differ from those in microporous media. At the same capillary number (10^{-3}), the viscous force dominates the entire displacement process in the no-slip microporous system. However, considering the slip effect in nanoporous systems, the displacement process may initially be dominated by the capillary force and then by the viscous force.

The inlet pressure continuously fluctuates under both slip and no-slip conditions, corresponding to complex interface dynamics within the nanoporous system. Figure 6B statistically analyzes the changes in water-oil volume flow rates under slip and no-slip conditions to predict complex flow processes. Significantly, water-oil flow rates fluctuate under both slip and no-slip conditions, indicating the complex pore filling events. Especially under no-slip conditions, the affinity of the pore surface for water and oil causes displacement to be sensitive to the pore topology, resulting in pronounced variations in water-oil flow rates. However, oil flow is free from the constraints of the pore surface under the slip condition, leading to enhanced mobility. This weakens the influence of interface dynamics associated with complex pore topology, resulting in smaller fluctuations in water-oil flow rates. Additionally, water-oil flow rates fluctuate significantly after the intersection points. This is mainly because the main terminal meniscus movement dominates the displacement process in the early stage, with the wetting fluid breaking through the outlet along dominant flow channels. Subsequently, wetting fluids displace oil in the form of film flow under the influence of interface tension force within blind-end pores and pore-throats with large aspect ratios, while arc menisci filling results in the trapping of non-wetting fluids.

Residual fluid distribution. The residual fluid distribution exhibits significant differences under slip and no-slip conditions, as displayed in Figure 7A. Wetting and non-wetting fluids are constrained by pore surfaces under no-slip conditions, with water films converging at narrow channels, resulting in a large amount of non-wetting fluid being trapped in blind-end pores. In contrast, the mobility of non-wetting fluid increases under the slip condition. Consequently, residual oil in blind-end pores and complex pore networks is easily displaced. Additionally, spherical residual oil resulting from snap-off events is observed under no-slip conditions. In comparison, snap-off events are less frequent under the slip condition, and the volume of spherical residual oil is reduced.

Wetting fluid is continuously injected into the complex pore system driven by external forces after the breakthrough. Therefore, fluid pressure decreases from the inlet to the outlet in Figure 7B. The pressure in regions with residual fluid distribution is higher, especially within blind-end pores. Under the no-slip condition, the large volume of residual oil increases the flow resistance of wetting fluids, and the pressure is larger. However, the pressure decreases due to reduced capture of non-wetting fluids under slip conditions. Correspondingly, the regions of pressure difference correspond to the regions of difference in residual fluid saturation under slip and no-slip conditions.

The simulated models exhibit lower residual oil saturation, fluid pressure, and interface curvature under slip conditions. Affected by the complex pore topology, there are certain differences in simulation results among the models. In Figure 7C, the residual fluid saturation ranges from 7.96% to 14.93% under no-slip conditions, while it ranges from 5.06% to 11.69% under slip conditions. Correspondingly, fluid pressure is decreased to different degrees considering slip effects, as illustrated in Figure 7D. In addition, the average interface curvature is positively correlated with residual fluid saturation in Figure 7E. Under no-slip conditions, the average interface curvature ranges from 19.39 to 33.68 μm^{-1}, while the interface curvature ranges from 15.18 to 31.95 μm^{-1} under slip conditions.

Effect of complex pore topology on flow characteristics. The pore topology affects the single-phase and two-phase water-oil flow. To quantitatively describe the complex pore topology, Figure S2 calculates the pore throat distribution characteristics using distance transformation and the watershed algorithm. The impact of pore topology on single-phase flow is analyzed. Since the consistent volume flow rate, significant differences in fluid pressure exist between slip and no-slip conditions. As displayed in Figure S2 A-C, the widespread distribution of narrow pore throat structures increases the flow resistance under slip and no-slip conditions (models C3 and C4), resulting in higher pressure for fluid flow. In contrast, the widely distributed large pores cause fluid to flow along the dominant channels, reducing the fluid pressure (model C1). Pore systems (model C2) exhibit strong pore connectivity with an extensive distribution of coordination numbers in Figure S2D, resulting in the lowest fluid pressure. In addition, the nanoporous systems with narrow structures exhibit higher pressure and velocity of no-slip flows (models C3 and C4), and the pressure drop for slip flow is pronounced due to confined spaces.

The influence of pore topology on two-phase water-oil flow and residual fluid saturation is further analyzed. Compared to no-slip flows, the residual oil saturation, fluid pressure, and interface curvature decrease under slip conditions. The effect of pore topology on pressure resembles that of single-phase flow. According to the pore throat distribution characteristics in Figure S2 A-C, pore systems with low porosity and a high proportion of small pores correspond to large displacement pressures (models C3 and C4). Strong pore connectivity reflected in Figure S2D reduces displacement pressure (model C2). Additionally, in poorly connected pore systems (model C1), the presence of a significant number of large pores allows water to flow along dominant pathways, resulting in lower pressure. Imbibition processes are dominated by capillary forces (models C1-C3) in the initial stage, achieving water saturation levels ranging from 8.34% to 15.77%. However, narrow pore throat structures inhibit imbibition (model C4), with significant contributions from viscous forces. Residual fluid distribution and interface curvature are closely related to pore topology. Pore systems with simple structures and strong connectivity correspond to satisfactory displacement effects (models C2 and C3). In contrast, pore systems with poor connectivity and narrow throat structures result in high residual oil saturation (models C1 and C4).

CONCLUSION

This work establishes a pore-scale model for nanoconfined multiphase flow in 3D clay nanopores of shale considering complex pore topology, slip flow, and capillary effects. Water/oil single-phase flow and water-oil forced imbibition simulations are conducted under the complete wetting condition. The microscopic force interactions, pore-filling mechanisms, and residual oil distribution are analyzed in 3D nanoporous media. The following conclusions are drawn:

(1) The flow of water in complete wetting nanoporous media is restricted, resulting in higher displacement pressure. However, the flow of oil is free from the constraints of pore surfaces, and the displacement pressure is extremely low. In addition, the velocity field under the slip condition is widely distributed and the inlet pressure is reduced by 4.7 times compared with that of no-slip flows.

(2) During the forced imbibition, the inlet pressure gradually increases under the slip condition and approaches the pressure under the no-slip condition. The displacement process may initially be dominated by the capillary force and then by the viscous force, resulting in water saturation reaching up to 15.7% with a negative inlet pressure. Due to the enhanced mobility of oil, the interface dynamics are relatively simple, resulting in reduced snap-off events, and the effective utilization of oil within blind-end pores.

(3) For the effect of pore structures, fluid flow experiences high pressure in pore systems with low porosity and narrow pore throat structures, while the pressure decreases significantly for slip flow. Residual oil saturation is positively correlated with interface curvature. Satisfactory displacement effects are observed in pore systems with simple structures and strong connectivity. Conversely, pore systems that exhibit poor connectivity and narrow throat structures tend to retain high residual oil saturation.

The developed EE-VOF model considering nanoscale slip effects restores the flow process in clay nanopores with complex pore topology. Affected by mineral composition, the wettability of shale reservoirs varies significantly, and even manifests as mixed wetting and heterogenous wetting. Although this simulation does not consider complex wettability conditions, it focuses on the flow processes under the complete wetting condition to highlight the slip effects. The microscopic force interactions and fluid trapping mechanisms are clarified for enhanced recovery.

REFERENCES

1. Zhu, Q., Wu, K., Guo, S., et al. (2024). Pore-scale investigation of CO2-oil miscible flooding in tight reservoir. Appl. Energy **368**:123439. DOI: https://doi.org/10.1016/j.apenergy.2024.123439.
2. Singh, H., Li, C., Cheng, P., et al. (2023). Automated real-time formation evaluation from cuttings and drilling data analysis: State of the art. Adv. Geo-Energy Res. **8**(1):19-36. DOI: https://doi.org/10.46690/ager.2023.04.03.
3. Hammouri, W., Guo, X., Abbas, M., et al. (2023). Nanopore evolution of the upper permian organic-rich shales from Dalong Formation, Sichuan Basin, during artificial hydrous pyrolysis. Energy Fuels **37**(10):7185-7200. DOI: https://doi.org/10.1021/acs.energyfuels.3c00752.
4. Bal, A., Misra, S., and Sen, D. (2024). Nanopore heterogeneity and accessibility in oil and gas bearing Cretaceous KG (Raghampuram) shale, KG Basin, India: An advanced multi-analytical study. Nat. Resour. Res. **33**(3):1131-1154. DOI: https://doi.org/10.1007/s11053-024-10319-3.
5. Wang, X., Meng, S., Ostadhassan, M., et al. (2024). Detecting shale oil hidden in nanopores using a novel electron microscopy method. The Innovation Energy **1**(1):100011. DOI: https://doi.org/10.59717/j.xinn-energy.2024.100011.
6. Liu, Q., Sun, M., Sun, X., et al. (2023). Pore network characterization of shale reservoirs through state-of-the-art X-ray computed tomography: A review. Gas Sci. Eng. **113**:204967. DOI: https://doi.org/10.1016/j.jgsce.2023.204967.
7. Fu, C., Xu, X., Du, Y., et al. (2024). Experimental study on the influence of pore structure on spontaneous imbibition in marine black shale. Capillarity **10**(3):57-72. DOI: https://doi.org/10.46690/capi.2024.03.01.
8. Wang, W., Xie, Q., Wang, H., et al. (2023). Pseudopotential-based multiple-relaxation-time lattice Boltzmann model for multicomponent and multiphase slip flow. Adv. Geo-Energy Res. **9**(2):106-116. DOI: https://doi.org/10.46690/ager.2023.08.04.
9. Cai, J., Jiao, X., Wang, H., et al. (2024). Multiphase fluid-rock interactions and flow behaviors in shale nanopores: A comprehensive review. Earth-Sci. Rev. **257**:104884. DOI: doi.org/10.1016/j.earscirev.2024.104884
10. Lukyanov, A.V., and Likhtman, A.E. (2016). Dynamic contact angle at the nanoscale: A unified view. ACS Nano **10**(6):6045-6053. DOI: doi.org/10.1021/acsnano.6b01630
11. Delle Piane, C., Ansari, H., Li, Z., et al. (2022). Influence of organic matter type on porosity development in the Wufeng-Longmaxi Shale: A combined microscopy,

neutron scattering and physisorption approach. Int. J. Coal Geol. 249:103880. DOI: https://doi.org/10.1016/j.coal.2021.103880.
12. Cai, J., Lin, D., Singh, H., et al. (2018). Shale gas transport model in 3D fractal porous media with variable pore sizes. Mar. Pet. Geol. 98:437-447. DOI: https://doi.org/10.1016/j.marpetgeo.2018.08.040.
13. Berg, S., Cense, A.W., Hofman, J.P., et al. (2008). Two-phase flow in porous media with slip boundary condition. Transp. Porous Media 74(3):275-292. DOI: https://doi.org/10.1007/s11242-007-9194-4.
14. Cheng, H., Wang, F., Guan, X., et al. (2023). A mathematical model for pre-Darcy flow in low permeability porous media with stress sensitivity and the boundary-layer effect. Eng. Geol. 324:107257. DOI: https://doi.org/10.1016/j.enggeo.2023.107257.
15. Cui, R., Hassanizadeh, S.M., and Sun, S. (2022). Pore-network modeling of flow in shale nanopores: Network structure, flow principles, and computational algorithms. Earth-Sci. Rev. 234:104203. DOI: https://doi.org/10.1016/j.earscirev.2022.104203.
16. Sun, H., Li, T., Li, Z., et al. (2023). Shale oil redistribution-induced flow regime transition in nanopores. Energy 282:128553. DOI: https://doi.org/10.1016/j.energy.2023.128553.
17. Wang, W., Xu, J., Zhan, S., et al. (2024). Multi-component oil–water two phase flow in quartz and kerogen nanopores: A molecular dynamics study. Fuel 362:130869. DOI: https://doi.org/10.1016/j.fuel.2024.130869.
18. Akhlaghi, H., Roohi, E., and Stefanov, S. (2023). A comprehensive review on micro- and nano-scale gas flow effects: Slip-jump phenomena, Knudsen paradox, thermally-driven flows, and Knudsen pumps. Phys. Rep. 997:1-60. DOI: https://doi.org/10.1016/j.physrep.2022.10.004.
19. Wang, H., Cai, J., Su, Y., et al. (2023). Imbibition behaviors in shale nanoporous media from pore-scale perspectives. Capillarity 9(2):32-44. DOI: https://doi.org/10.46690/capi.2023.11.02.
20. Wu, K., Chen, Z., Li, J., et al. (2017). Wettability effect on nanoconfined water flow. Proc. Natl. Acad. Sci. U.S.A. 114(13):3358-3363. DOI: https://doi.org/10.1073/pnas.1612608114.
21. Wang, G., Chen, X., Wang, S., et al. (2022). Influence of fracture connectivity and shape on water seepage of low-rank coal based on CT 3D reconstruction. J. Nat. Gas Sci. Eng. 102:104584. DOI: https://doi.org/10.1016/j.jngse.2022.104584.
22. Cudjoe, S.E., Barati, R., Tsau, J.S., et al. (2021). Assessing the efficiency of saturating shale oil cores and evaluating hydrocarbon gas huff 'n' puff using nuclear magnetic resonance. SPE Res. Eval. Eng. 24(02):429-439. DOI: https://doi.org/10.2118/205027-PA.
23. Lin, Z., Hu, Q., Yin, N., et al. (2024). Nanopores-to-microfractures flow mechanism and remaining distribution of shale oil during dynamic water spontaneous imbibition studied by NMR. Geoenergy Sci. Eng. 241:213202. DOI: https://doi.org/10.1016/j.geoen.2024.213202.
24. Bao, B., and Zhao, S. (2021). A review of experimental nanofluidic studies on shale fluid phase and transport behaviors. J. Nat. Gas Sci. Eng. 86:103745. DOI: https://doi.org/10.1016/j.jngse.2020.103745.
25. Zhang, Y., Dou, S., Qi, J., et al. (2022). Experimental study on slip flow of nitrogen through microchannels at atmospheric pressure. Microfluid. Nanofluid. 27(2):7. DOI: https://doi.org/10.1007/s10404-022-02616-1.
26. Sun, S., Liang, S., Liu, Y., et al. (2023). A review on shale oil and gas characteristics and molecular dynamics simulation for the fluid behavior in shale pore. J. Mol. Liq. 376:121507. DOI: https://doi.org/10.1016/j.molliq.2023.121507.
27. Ramisetti, S.B., and Yadav, A. (2022). Insights from molecular simulations on liquid slip over nanostructured surfaces. J. Mol. Model. 28(11):346. DOI: https://doi.org/10.1007/s00894-022-05338-x.
28. Fernández-Fidalgo, J., Cueto-Felgueroso, L., Ramírez, L., et al. (2024). Pore-scale simulation of multiphase flows using equations of state that preserve the correct surface tension. Comput. Methods Appl. Mech. Eng. 428:117072. DOI: https://doi.org/10.1016/j.cma.2024.117072.
29. Khoshtarash, H., Siavashi, M., Ramezanpour, M., et al. (2023). Pore-scale analysis of two-phase nanofluid flow and heat transfer in open-cell metal foams considering Brownian motion. Appl. Therm. Eng. 221:119847. DOI: https://doi.org/10.1016/j.applthermaleng.2022.119847.
30. Song, W., Yao, J., Zhang, K., et al. (2022). Nano-scale multicomponent hydrocarbon thermodynamic transport mechanisms in shale oil reservoir. J. Pet. Sci. Eng. 219:111093. DOI: https://doi.org/10.1016/j.petrol.2022.111093.
31. Yang, J., Xu, Q., Kou, X., et al. (2024). Three-dimensional pore-scale study of methane hydrate dissociation mechanisms based on micro-CT images. The Innovation Energy 1(1):100015. DOI: https://doi.org/10.59717/j.xinn-energy.2024.100015.
32. Yang, Y., Wang, K., Zhang, L., et al. (2019). Pore-scale simulation of shale oil flow based on pore network model. Fuel 251:683-692. DOI: https://doi.org/10.1016/j.fuel.2019.03.083.
33. Wang, H., Su, Y., and Wang, W. (2022). Improved lattice Boltzmann method to simulate liquid flow in nanoporous media: Coupling molecular dynamics simulations and theoretical model. Adv. Water Resour. 165:104239. DOI: https://doi.org/10.1016/j.advwatres.2022.104239.
34. Qin, X., Wu, J., Xia, Y., et al. (2024). Multicomponent image-based modeling of water flow in heterogeneous wet shale nanopores. Energy 298:131367. DOI: https://doi.org/10.1016/j.energy.2024.131367.
35. Sun, C., Tang, K., Zhou, R., et al. (2024). Two-phase imbibition of water-oil displacement in silica nanochannels. Int. J. Multiphase Flow 172:104710. DOI: https://doi.org/10.1016/j.ijmultiphaseflow.2023.104710.
36. Wang, R., Chai, J., Luo, B., et al. (2021). A review on slip boundary conditions at the nanoscale: recent development and applications. Beilstein J. Nanotechnol. 12:1237-1251. DOI: https://doi.org/10.3762/bjnano.12.91.
37. Singh, K., Bultreys, T., Raeini, A.Q., et al. (2022). New type of pore-snap-off and displacement correlations in imbibition. J. Colloid Interface Sci. 609:384-392. DOI: https://doi.org/10.1016/j.jcis.2021.11.109.
38. Alhosani, A., Scanziani, A., Lin, Q., et al. (2020). Dynamics of water injection in an oil-wet reservoir rock at subsurface conditions: Invasion patterns and pore-filling events. Phys. Rev. E 102(2):023110. DOI: https://doi.org/10.1103/PhysRevE.102.023110.
39. Foroughi, S., Bijeljic, B., and Blunt, M.J. (2021). Pore-by-pore modelling, validation and prediction of waterflooding in oil-wet rocks using dynamic synchrotron data. Transp. Porous Media 138(2):285-308. DOI: https://doi.org/10.1007/s11242-021-01609-y.
40. Zhang, W., Feng, Q., Wang, S., et al. (2022). Pore network modeling of oil and water transport in nanoporous shale with mixed wettability. J. Pet. Sci. Eng. 209:109884. DOI: https://doi.org/10.1016/j.petrol.2021.109884.
41. Zhang, T., Javadpour, F., Li, J., et al. (2021). Pore-scale perspective of gas/water two-phase flow in shale. SPE J. 26(02):828-846. DOI: https://doi.org/10.2118/205019-PA.
42. Wang, H., Wang, W., Su, Y., et al. (2022). Lattice Boltzmann model for oil/water two-phase flow in nanoporous media considering heterogeneous viscosity, liquid/solid, and liquid/liquid slip. SPE J. 27(06):3508-3524. DOI: https://doi.org/10.2118/210564-PA.
43. Liu, H., Zhang, W., Jia, M., et al. (2018). An improved method for coupling the in-nozzle cavitation with Multi-fluid-quasi-VOF model for diesel spray. Comput. Fluids 177:20-32. DOI: https://doi.org/10.1016/j.compfluid.2018.09.017.
44. Ambekar, A.S., Mondal, S., and Buwa, V.V. (2021). Pore-resolved volume-of-fluid simulations of two-phase flow in porous media: Pore-scale flow mechanisms and regime map. Phys. Fluids 33(10):102119. DOI: https://doi.org/10.1063/5.0064833.
45. Huang, D.M., Sendner, C., Horinek, D., et al. (2008). Water slippage versus contact angle: A quasiuniversal relationship. Phys. Rev. Lett. 101(22):226101. DOI: https://doi.org/10.1103/PhysRevLett.101.226101.
46. Chen, Y., Wang, L., Chang, H., et al. (2023). A review of drag coefficient models in gas-liquid two-phase flow. Chem. Bio. Eng. Rev. 10(3):311-325. DOI: https://doi.org/10.1002/cben.202200034.
47. Zhao, J., Kang, Q., Yao, J., et al. (2018). Lattice Boltzmann simulation of liquid flow in nanoporous media. Int. J. Heat Mass Transfer 125:1131-1143. DOI: https://doi.org/10.1016/j.ijheatmasstransfer.2018.04.123.
48. Zhu, G., Yao, J., Zhang, L., et al. (2016).Investigation of the dynamic contact angle using a direct numerical simulation method. Langmuir 32(45):11736-11744. DOI: https://doi.org/10.1021/acs.langmuir.6b02543.
49. Liu, Y., Chen, M., Sun, S., et al. (2022). Effects of grain shape and packing pattern on spontaneous imbibition under different boundary conditions: Pore-scale simulation. J. Hydrol. 607:127484. DOI: https://doi.org/10.1016/j.jhydrol.2022.127484.
50. Dong Sung, K., Kwang-Cheol, L., Tai Hun, K., et al. (2002). Micro-channel filling flow considering surface tension effect. J. Micromech. Microeng. 12(3):236. DOI: https://doi.org/10.1088/0960-1317/12/3/307.
51. Liu, Y., Berg, S., Ju, Y., et al. (2022). Systematic investigation of corner flow impact in forced imbibition. Water Resour. Res. 58(10):e2022WR032402. DOI: https://doi.org/10.1029/2022WR032402.

FUNDING AND ACKNOWLEDGMENTS

The funders had no role in study design, data collection and analysis, decision to publish, or preparation of the manuscript. This work was supported by the National Natural Science Foundation of China (Nos. 42172159, and 42302143), and the Science Foundation of China University of Petroleum, Beijing (No. 2462023XKBH009).

AUTHOR CONTRIBUTIONS

Xiangjie Qin: Methodology, Software, Supervision, Validation, Writing. Han Wang: Methodology, Software, Supervision. Yuxuan Xia: Methodology, Investigation. Wu He: Software, Methodology, Conceptualization. Xuanzhe Xia: Formal analysis, Review and editing. Jianchao Cai: Methodology, Funding acquisition, Review and editing.

DECLARATION OF INTERESTS

The authors declare no competing interests.

DATA AND CODE AVAILABILITY

Data are available from the corresponding author upon reasonable request.

SUPPLEMENTAL INFORMATION

Supplementary material is available at: https://doi.org/10.59717/j.xinn-energy.2024.100050